npj | computational materials

Article

Published in partnership with the Shanghai Institute of Ceramics of the Chinese Academy of Sciences

https://doi.org/10.1038/s41524-024-01361-z

Low-symmetry vacancy-related spin qubit in hexagonal boron nitride

Rohit Babar[1,2,9], **Gergely Barcza**[1,2,9], **Anton Pershin**[1,3,9], **Hyoju Park**[4], **Oscar Bulancea Lindvall**[5], **Gergő Thiering**[1], **Örs Legeza**[1,6], **Jamie H. Warner**[4], **Igor A. Abrikosov**[5], **Adam Gali**[1,3,7] & **Viktor Ivády**[2,5,8]

Point defect qubits in semiconductors have demonstrated their outstanding capabilities for high spatial resolution sensing generating broad multidisciplinary interest. Hexagonal boron nitride (hBN) hosting point defect qubits have recently opened up new horizons for quantum sensing by implementing sensing foils. The sensitivity of point defect sensors in hBN is currently limited by the linewidth of the magnetic resonance signal, which is broadened due to strong hyperfine couplings. Here, we report on a vacancy-related spin qubit with an inherently low symmetry configuration, the VB2 center, giving rise to a reduced magnetic resonance linewidth at zero magnetic fields. The VB2 center is also equipped with a classical memory that can be utilized for storing population information. Using scanning transmission electron microscopy imaging, we confirm the existence of the VB2 configuration in free-standing monolayer hBN.

In the new era of quantum sensing, point defect qubits play a crucial role in revolutionizing measurements in material science, biology, and medicine[1]. In particular, the NV center in diamond[2] has provided the means to detect magnetic field[3], electric field[4], strain[5], and temperature[6] with high spatial resolution and high sensitivity. Novel magnetic resonance protocols[7,8] with unlimited frequency resolution[9,10] have opened new horizons for magnetic resonance in the few-spin limit that provides hitherto inaccessible information on the structure and functioning of molecules and proteins[11]. On the other hand, the NV center is an inherently bulk system, that implies severe challenges when near-surface applications are demanded[12,13]. Wide-band gap van der Waals semiconductors with mature exfoliation possibilities, such as hBN, hosting applicable, optically addressable point defect qubits on the surface and even in a single layer may be advantageous in various sensing applications[14,15]. Recently, hBN sensing foils have been utilized to detect the magnetic field of van der Waals heterostructures[16,17], paramagnetic defects[18,19], and other nanometer-scale structures[20].

Optically detected magnetic resonance (ODMR) studies have demonstrated optically addressable spin qubits in hBN[21–25]. One of the qubits has already been assigned to the negatively charged boron vacancy (V_B center)[22,26–28]. The VB center can be coherently manipulated[29,30] and used as high spatial resolution thermometer[31] and magnetic field probe[16–20]. The sensitivity of these sensors, however, falls most often behind the NV center in diamond[31]. The reasons for the relatively low sensitivity of the V_B center are the low photon emission rate due to the first-order forbidden optical transition[26] and the noisy environment due to the 100% natural abundance of paramagnetic isotopes of B and N. Other ODMR centers in hBN exhibit narrow linewidth[23–25,32] and bright optical signals, however, their microscopic structures are yet to be explored. While these centers are promising for quantum sensing[23,25], their controlled fabrication on an ensemble level has not been achieved.

Recent developments in the field of single-photon emitters and qubits in hBN have inspired a vast number of theoretical studies[32–42]. In contrast to conventional bulk systems, such as diamond and silicon carbide (SiC), point defect related electronic states in hBN are often strongly correlated and require treatment on high level of theory[28,43]. Fortunately, the layered structure of the hBN allows computationally affordable but physically sound models to be studied by advanced post-DFT and post-Hartree-Fock

---

[1]HUN-REN Wigner Research Centre for Physics, PO Box 49, H-1525 Budapest, Hungary. [2]MTA-ELTE Lendület “Momentum” NewQubit Research Group, Pázmány Péter, Sétány 1/A, 1117 Budapest, Hungary. [3]Department of Atomic Physics, Insitute of Physics, Budapest University of Technology and Economics, Műegyetem rakpart 3., H-1111 Budapest, Hungary. [4]Walker Department of Mechanical Engineering and Materials Graduate Program, Texas Materials Institute, The University of Texas at Austin, Austin, TX, 78712, USA. [5]Department of Physics, Chemistry and Biology, Linköping University, SE-581 83 Linköping, Sweden. [6]Institute for Advanced Study, Technical University of Munich, Lichtenbergstrasse 2a, 85748 Garching, Germany. [7]MTA-WFK Lendület “Momentum” Semiconductor Nanostructures Research Group, PO Box 49, H-1525 Budapest, Hungary. [8]Department of Physics of Complex Systems, Eötvös Loránd University, Egyetem tér 1-3, H-1053 Budapest, Hungary. [9]These authors contributed equally: Rohit Babar, Gergely Barcza, Anton Pershin. e-mail: gali.adam@wigner.hu; ivady.viktor@ttk.elte.hu

methods[28,43]. Such methods enable us to carry out predictive, quantitatively accurate computational studies in hBN[26,44].

Here we experimentally and computationally investigate a point defect complex created by the fusion of two boron vacancies in the neutral charge state. We demonstrate by scanning transmission electron microscopy (STEM) imaging that the stable configuration of the defect, named VB2 center, can be found in single-layer free-standing hBN samples after electron irradiation. We report on nearly degenerate singlet-triplet pairs of states in the spectrum of the defect with allowed optical transitions for initializing and reading out the spin states. We show that the peculiar electronic structure of the VB2 configuration enables long-lived storage of population information in the singlet manifold. Furthermore, we demonstrate that the transverse zero-field splitting interaction of the ground state gives rise to efficient coherence protection mechanisms. As a result, the electron spin resonance linewidth is reduced by a factor of 4.2, and the inhomogeneous coherence time is elongated by a factor of 7.5 at zero magnetic fields compared to those obtained at non-zero magnetic field values. The reported properties of the VB2 center may be utilized in novel quantum sensing applications with high sensitivity.

Results

Structure, stability, and fabrication

A pair of adjacent in-plane boron vacancies results in a highly unstable configuration where the nitrogen atom between the two vacancies possesses two dangling bonds and binds only to a single boron atom, see Fig. 1a. The loosely bonded nitrogen atom between the boron vacancies migrates into one of the vacancy sites. A new point defect complex is formed consisting of a boron vacancy, a nitrogen vacancy, and a nitrogen anti-site ($V_BV_NN_B$). One of the six possible symmetrically equivalent configurations is depicted in Fig. 1b, while the remaining five configurations can be obtained by rotating this structure 120° and 240° around an outplane axis, as well as reflecting the original and rotated configurations to perpendicular of plane reflection planes. The $V_BV_NN_B$ defect complex is from now on refered to as the VB2 configuration. Due to the formation of strong nitrogen-nitrogen bonds in the VB2 configuration, the complex is highly favorable. Indeed, the binding energy of two boron vacancy pairs is found to be as large as 5.15 eV in good agreement with the previous theoretical prediction of 4.9 eV[45]. The small difference in the theoretical values can be attributed to the use of different hybrid functionals in the calculations.

The formation energy curves of the VB2 and the V_B defects as a function of the Fermi energy are depicted in Fig. 1c. The figure demonstrates that the VB2 configuration exhibits four stable charge states and three charge-state transition levels, $(+1/0)$, $(0/-1)$, and $(-1/-2)$ at 1.78 eV, 3.61 eV, and 4.90 eV in the band gap of hBN, respectively. The neutral charge state is stable in the middle of the band gap and photostable up to 3.61 eV photon energy, which is the threshold for exciting an electron from the valence band to the defect and creating a negatively charged VB2 configuration and a hole at the valence band edge, see Fig. 1c.

To confirm the existence and stability of the VB2 configuration in hBN, we carry out annular dark-field scanning transmission electron microscopy (ADF-STEM) imaging of a single-layer free-standing hBN sample grown in our CVD laboratory[46]. Among many other defect types reported in previous works[46], our experiments reveal here the VB2 defect in single layer hBN, see Fig. 1d. The STEM image of the VB2 configuration resembles the boron vacancy-nitrogen vacancy complex, however, the intensity profile across the bright atoms shows an excellent match to the VB2 complex with an adjacent

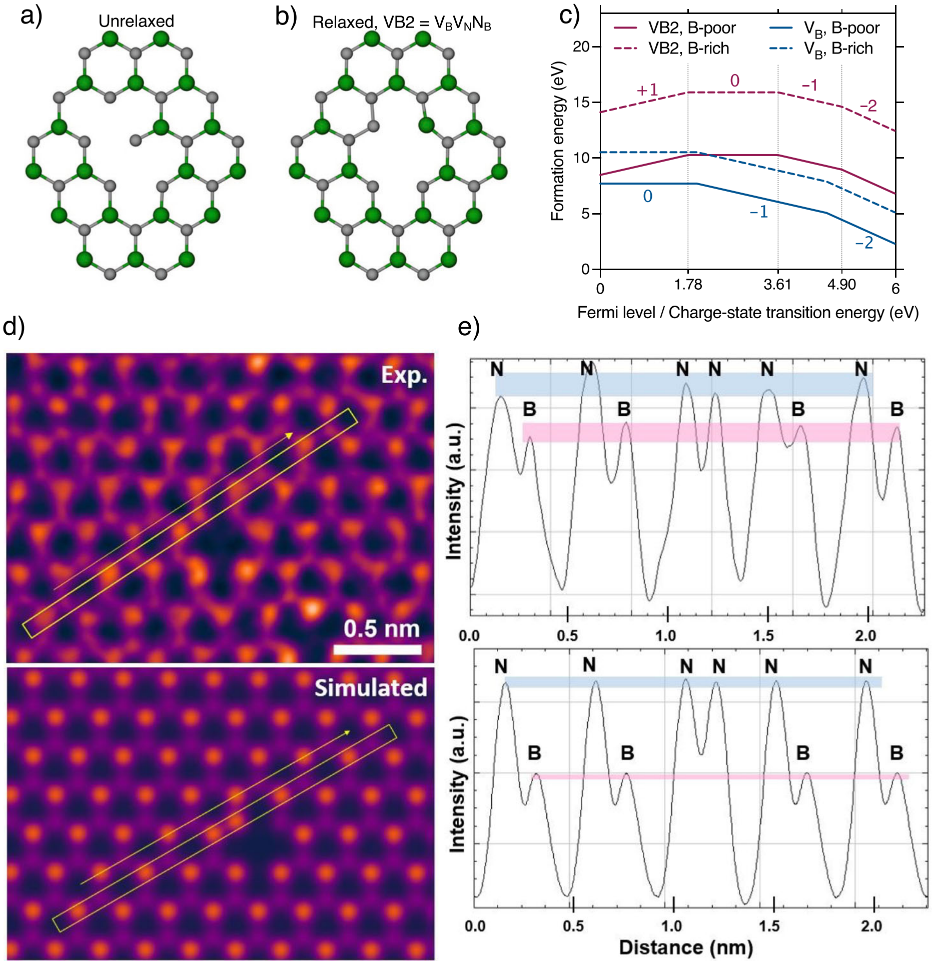

Fig. 1 | Structure and stability of the VB2 center. **a** Unrelaxed structure of two adjacent boron vacancies. **b** The energetically most favorable VB2 configuration where the unstable nitrogen atom of two dangling bonds has jumped into the upper boron vacancy site forming a $V_BV_NN_B$ complex. **c** Formation energies of VB2 (magenta) and V_B (light blue) defects in h-BN as a function of Fermi level under B-poor (solid line) and B-rich (dashed line) growth conditions. Color-coded numbers represent the charge states of the corresponding defect, while vertical dotted gray lines indicate the charge state transition levels of the VB2 defect. **d** A false-coloured ADF-STEM image of the VB2 configuration in single layer free-standing hBN sample. The top and bottom panels show the experiment and simulation of the VB2 configuration. **e** Intensity profile across the bright atoms along the yellow dashed box in **d** that reveals an anti-site nitrogen next to the vacancy sites.

pair of N atoms in the first neighbor shell of the vacancies, see the multi-slice simulated STEM image in Fig. 1e.

We note that the appearance of the VB2 configuration is presumably a consequence of the high-energy electron irradiation of the STEM imaging. In our measurements, clean defect-free regions of the suspended hBN monolayers were first located on a layer carbon Cu mesh TEM grid. Because hBN reacts under the electron beam, vacancies and defects are produced during imaging. The creation of defects is stochastic, however, more likely boron vacancies are formed. In addition, prior work has shown that electron beam irradiation of monolayer hBN causes the ejection of B and N atoms around point defects leading to defect complex formation[46]. The observed VB2 defect is presumably the result of the high-energy non-equilibrium processes taking place under the STEM measurements and not an ingrown defect. Elaborating further on this observation, we note that the STEM may utilized for high-position accuracy fabrication of defects, including the VB2 configuration, e.g. by using engineered electron beam pulses at specific locations and omitting scanning of the sample. Filling of vacancies with other adventitious atoms is also possible, such as C or O, coming from the TEM column vacuum chamber[46]. For further discussion on the single layer and bulk fabrication see Supplementary Note 2 with Supplementary References[34,45,47–51].

Observation of the VB2 configuration in our STEM images motivates an in-depth study of the excited states and magneto-optical properties of the defect, which is the topic of the following sections.

Excited state properties

The in-plane and perpendicular-to-plane dangling bonds of the VB2 configuration give rise to a number of localized defect states, most of which can be found in the band gap of hBN. For a comprehensive analysis of the single-particle electronic structure, see Supplementary Note 3. As a consequence of the complicated electronic structure, several excited states can be found below the ionization threshold resulting in diverse optical excitation and decay pathways.

The energy level spectrum including the eight lowest-lying many-particle energy levels obtained on corresponding relaxed geometries is depicted in Fig. 2a. The spectrum exhibits a peculiar feature that has not been seen in point defect qubits before, i.e. it is built up from nearly degenerate pairs of singlet and triplet states, referred to as excited manifolds from now on. The reason for the observed quasi-degenerate singlet-triplet pairs can be understood by examining the ground state triplet. Due to the defect's low symmetry, the observed high-spin ground state is the result of an accidental degeneracy in the single-particle electronic structure, see Supplementary Note 3. The unpaired electrons occupy two defect states that belong to two different irreducible representations and are localized on distinct first neighbor atoms of the defect, see the spin density in Fig. 3a. As a result, the exchange energy is marginal in the ground state and gives rise only to a 3.3 meV splitting between the ground state triplet and the corresponding lowest energy singlet state. The wavefunctions of the low energy optical excited states exhibit similar characteristics that explain the spectrum depicted in Fig. 2a.

Since the triplet and singlet states in each manifold have approximately the same spatial wavefunctions and atomic configurations, spin-orbit coupling and phonon-mediated inter-system crossing (ISC) between these states are forbidden in leading order (El-Sayed's rule). Consequently, the lowest lying S0 singlet excited state close to the triplet ground state T0 is long-lived. Indeed, we find the lifetime of the S0 state to be as long as 39.5 ms at low temperatures, which remains in the same order of magnitude even at room temperature. This indicates that the S0 singlet state can serve as a classical memory to store population information.

By analyzing the potential decay pathways from the excited states, we find that the states in the lowest-lying ES1 manifold can directly decay non-radiatively to the ground state, and its lifetime is expected to be in the picosecond range, see Supplementary Note 4 with Supplementary References[52–57]. The fast decay suppresses any optical emission from the T1 triplet and S1 singlet states. On the other hand, the ES2 manifold is optically active and gives rise to zero-phonon luminescence (ZPL) lines from the T2 triplet and the S2 singlet states at 1.578 eV and 1.586 eV, respectively. We note color centers most often emit from the lowest energy excited state, however, depending on the ratio of the radiative and phonon-assisted non-radiative decay rates, higher-lying excited states may also be optically active[58]. High-temperature PL spectrum of the VB2 defect is depicted in Fig. 2b showing a 60 nm red-shifted PL phonon side-band compared to the boron vacancy center. The ES3 manifold decays dominantly to the ES2 manifold via internal conversion.

Figure 2c depicts the most relevant radiative and non-radiative decay pathways of the VB2 defect. Besides the optical decay, the system can decay non-radiatively from the ES2 manifold through the ES1 manifold to the ground state manifold by emitting phonons. For the quantum efficiency of the VB2 center, we obtain 0.15 and 0.12 for the triplet and the singlet transitions, respectively. The inter-system crossing (ISC) rates between the singlet and triplet channels are a few orders of magnitude smaller than the spin-conserving decay rates, see Fig. 2c. Consequently, the singlet and triplet emissions are independent of each other to a large degree. This effect and the differences in the optical lifetime and the emission energy of the T2 triplet and the S2 singlet states can be utilized to realize a single-shot read-out of the singlet-triplet occupation, see Supplementary Note 4 for more details.

Since the electronic structure of the VB2 configuration does not exhibit dark long-lived metastable states, the photon count observed in the

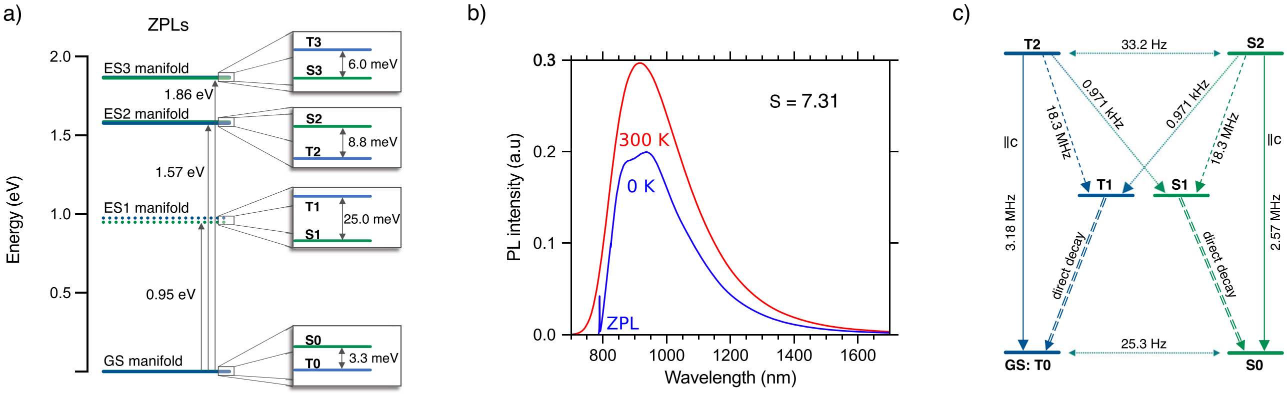

Fig. 2 | Optical properties, initialization, and non-destructive readout of the VB2 center. **a** Energy level structure of the VB2 defect exhibiting quasi degenerate singlet-triplet pairs throughout the spectrum. **b** Calculated PL emission spectra of the VB2 defect a room temperature. The emission maximum is red-shifted by 60 nm compared to the PL emission peak of the V_B center. **c** Schematic diagram of the possible radiative and phonon-assisted non-radiative relaxation pathways. Solid arrows indicate optical transition with parallel to *c*-axis polarization, dashed arrows indicate spin-conserving non-radiative relaxation, dashed double line arrows indicate direct spin-conserving relaxation to the ground state, and dotted arrows indicate spin non-conserving non-radiative transitions through inter-system crossings.

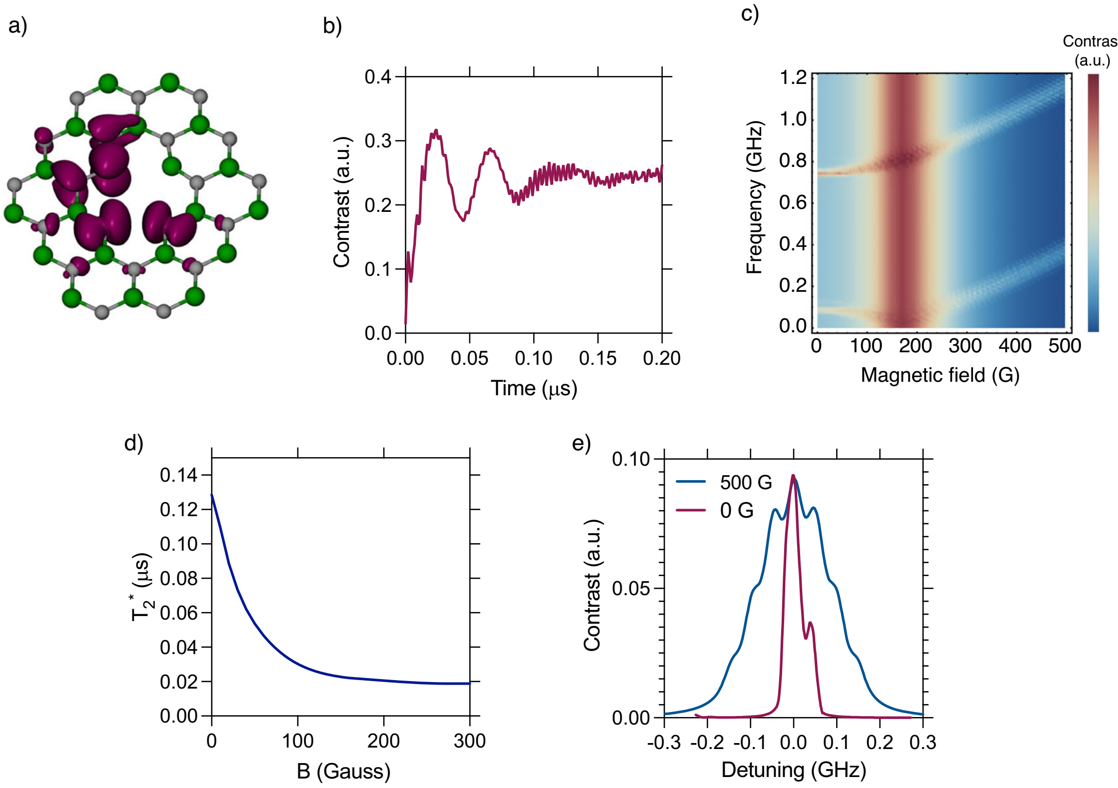

Fig. 3 | Qubit properties of the VB2 center. a Spin density of the triplet ground state of VB2 center. **b** Rabi oscillation of the electron spin at zero magnetic fields. **c** Magnetic resonance map of the VB2 center as a function of the applied magnetic field (horizontal axis) and the microwave frequency (vertical axis). In the simulations, the system was driven by an in-plane polarized microwave field. The broad frequency-independent signal at 160 G is due to the hyperfine mixing of the spin states observed at the level avoided-crossing of the electron spin levels. **d** Magnetic field dependence of the free induction decay time (T_2^*). The coherence time is enhanced by a factor of 7.5 close to $B = 0$ due to the transverse zero-field splitting that partially suppresses the hyperfine coupling. **e** Magnetic resonance signal at 0 G and 500 G magnetic field values. The width of the zero-field electron spin resonance signal is 23.8% of the width of the signal at 500G. This effect gives rise to a 4.2 times enhancement of the sensitivity at zero magnetic field.

measurements is limited by the radiative lifetime, two-photon excitation processes, and collection efficiency of the emitted photons in saturation. Due to the high photon collection efficiency achievable in hBN[59,60] and the ≈ 3 MHz radiative lifetime of the VB2 center, the saturated photo-count of a single VB2 center is expected to be in the order of 100 kcps.

The ISC transition between the singlet and triplet states is found to be strictly selective on the spin sub-levels of the triplet states, i.e. only the $|m_S = 0\rangle$ state is connected with the singlet channel. Consequently, continuous optical excitation of the VB2 center leads to spin polarization in the triplet ground state. Furthermore, since the triplet and singlet radiative relaxation rates are slightly different in the ES2 manifold, see Fig. 2c, the luminescence of the VB2 defect depends on the spin state. The saturated spin read-out contrast is approximated to be 4.6%, see Supplementary Note 4. Since the contrast is set by the relative luminescence intensity of the singlet and triplet manifolds, for which we do not expect considerable temperature dependence, and not by the relative rates of various non-radiative decay processes, the observed 4.6% contrast may be preserved even at room temperature. Finally, we note that fast ISC transitions and fast optical spin initialization may be achieved by pumping through the ES3 manifold, where ISC rates are found in the MHz range. Such excitation, on the other hand, may not be advantageous for read-out due to the enhanced non-radiative decay rates that may substantially reduce the quantum efficiency of the defect.

VB2 center as a qubit

As we have shown, the spin states of the ground state triplet of the VB2 center can be initialized and read out optically, therefore the spin states of the defect complex can implement an optically addressable qubit in hBN. In the following, we study the spin and qubit properties of the center. Figure 3a depicts the spin density of the triplet ground state that clearly shows low symmetric characteristics, in contrast to existing point defect qubits that exhibit (quasi-)three-fold rotation symmetry. The spin Hamiltonian of the triplet ground state is discussed in Supplementary Note 5 with Supplementary References[47,61,62].

The low symmetric structure has a significant effect on the zero-field splitting (ZFS) interaction whose preferential quantization axis is in-plane and the corresponding conventional ZFS parameters are $D = 1.394$ GHz and $E = 78.2$ MHz. Note, however, that the preferential quantization axis of the spin-orbit interaction is perpendicular to the plane. Hereinafter, we use this latter quantization axis, in which the electron spin is polarized in the $|m_S = 0\rangle = |0\rangle$ spin state. In this basis, a new set of non-conventional ZFS parameters can be defined as $\widetilde{D} = -814$ MHz and $\widetilde{E} = -658$ MHz that provides the same level structure as the conventional ZFS parameters in the corresponding quantization basis. Here, we note that due to the six possible orientations of the defects with six different preferential quantization axes, one would observe a complex magnetic field-dependent ODMR signal in an ensemble.

The large effective transverse ZFS $\widetilde{E}$ mixes the $|m_S = \pm 1\rangle = |\pm 1\rangle$ spin states and gives rise to new quantum states $|\pm\rangle = |+1\rangle \pm |-1\rangle$. By applying a microwave field that is polarized in an in-plane direction, spin transitions can be resonantly driven between the $|0\rangle$ and $|\pm\rangle$ state at zero magnetic fields. Rabi oscillation can be observed in the optical signal due to the microwave drive, see Fig. 3b. In Fig. 3c, we depict the magnetic field dependence of the resonance signal. As the magnetic field enhances the zero-field mixing of the $m_S = \pm 1$ states reduces; the states become the eigenstates of the Zeeman Hamiltonian term, and eventually depend linearly on the magnetic field. On the other hand, as can be seen in Fig. 3c, the spin states are independent of the magnetic field in first order at $B \approx 0$. The zero first-order Zeeman (ZEFOZ) transitions arising at this field are protected from magnetic fluctuations that result in an elongated coherence time of the qubit states. We study this effect through the magnetic field dependence of the free induction decay time ($T_2^\star$) in Figure 3d. As can be seen, the coherence time is enhanced by a factor of 7.5 at $B = 0$ and reaches a value as high as 128 ns. Note that the coherence time may be further elongated by driving a transition between $|+\rangle$ and $|-\rangle$ states with a parallel to plane-polarized microwave field. These coherence protection schemes are indispensable in hBN as it possesses nuclear spins in its lattice with 100% natural abundance. We note furthermore that the electron spin resonance linewidth is reduced by a factor of 4.2 at zero magnetic fields, see Fig. 3e.

Note, furthermore, that the magnetic resonance map in Fig. 3c exhibits a broad driving frequency-independent signal at $B \approx 160$ G. This signal is due to hyperfine coupling of the environment whose effect is enhanced at the avoided-crossing of the ground state spin levels observed at $B \approx 160$ G, see Supplementary Note 5. The interplay of the optical pumping and the strong hyperfine coupling at this magnetic field may give rise to efficient polarization of the surrounding spin bath. Low magnetic field hyperpolarization of an hBN sample can be utilized in sensitivity-enhanced NMR and MRI measurements[63].

VB2 as a sensor

Finally, we study the sensitivity of the VB2 center. To this end, we first determine the pressure and electric field dependence of the ZFS parameters, for which we obtain $d\widetilde{D}/dp = 9.98$ MHz/kBar (-8.61 MHz/kBar) and $d\widetilde{E}/dp = 8.50$ MHz/kBar (-9.36 MHz/kBar) for pressure applied parallel (perpendicular) to the $\mathrm{V_B}$-$\mathrm{V_N}$ axis and $d\widetilde{D}/d\mathcal{E} = 0.04$ Hz cm/V (-3.45 Hz cm/V) and $d\widetilde{E}/d\mathcal{E} = 3.81$ Hz cm/V (7.52 Hz cm/V) for static electric field $\mathcal{E}$ set parallel (perpendicular) to the $\mathrm{V_B}$-$\mathrm{V_N}$ axis. The stress coupling parameters of the VB2 center and the $\mathrm{V_B}$ center[31] are comparable, however, they are two orders of magnitude larger than the NV center's stress coupling parameter[64]. The electric field coupling parameter of the VB2 center along special directions is comparable to the NV center's electric field coupling strength.

The shot noise limited sensitivity of a single VB2 sensor in continuous wave magnetic resonance measurement scheme can be obtained according to the formula[65,66]

$$\eta_{\mathrm{MR}} = \left(\frac{d\nu_{0+}}{d\mathcal{P}}\right)^{-1} \frac{\Delta\nu}{C\sqrt{\mathcal{R}}}\,, \tag{1}$$

where ν_{0+} is the resonance frequency, $\mathcal{P}$ is the perturbation to be measured, $\Delta\nu$ is the full width at half maximum of the magnetic resonance curve, which takes 49.5 MHz at zero magnetic fields for electric field, pressure, and temperature sensing and 205 MHz at high magnetic field values for DC magnetic field sensing, $C \approx 0.05$ is the estimated spin read-out contrast, and $\mathcal{R}$ is the photon count that may reach 100 kcps in saturation. Using this formula and the values specified above, for pressure, DC electric field, and DC magnetic field sensitivity we respectively obtain 30 MPa/Hz$^{1/2}$, 907 kV/cm/Hz$^{1/2}$, and 463 μT/Hz$^{1/2}$ for a single VB2 defect in hBN in continuous wave sensing mode.

Discussion

The sensitivity of the VB2 center in a continuous wave measurement scheme is expected to be lower than that of the NV center in diamond, dominantly due to the enhanced magnetic resonance linewidth and the slightly lower photon count of the VB2 center. On the other hand, it may still be useful for high spatial resolution sensing in near-surface and low-dimension applications. The dipole-allowed optical transition, the sizable spin read-out contrast, and the narrowed-down magnetic resonance signal at zero magnetic fields are all in favor of the VB2 center.

Pulsed sensing protocols and decoherence protection techniques can be utilized to enhance the sensitivity of the VB2 center further. The low symmetric structure offers new functionalities. The long-lived bright singlet manifold can be utilized as a memory and may lead to the storage of spin state population information beyond the spin relaxation time of the ground state triplet. This may be utilized in a single-shot read-out of the spin states when the center is coupled with an optical cavity. Furthermore, dressing of the $|\pm\rangle$ states with resonant microwave drive may be used in filtering out low-frequency magnetic field fluctuations[62] that can give rise to a highly protected subspace in hBN.

Fabrication of point defect qubits in 2D materials offers new possibilities in nanometer-scale sensing. For example, few-layer hBN samples with pre-fabricated sensors may be moved on top of nano-scale structures or installed in van der Waals heterostructure in order to obtain high spatial resolution information not accessible with other means. The VB2 center exhibiting desirable qubit properties has already been fabricated in single-layer hBN providing a suitable sensor for such applications.

In summary, in this joint theoretical and experimental work, we investigated the peculiar properties of the neutrally charged VB2 configuration in hBN. The appearance of this structural defect has been demonstrated in our STEM measurements on a free-standing single-sheet hexagonal boron nitride sample. We showed that the triplet ground state of the VB2 defect implements an optically addressable spin qubit with novel characteristics. The possibility of an efficient coherence protection mechanism and dipole-allowed optical transition makes the VB2 center a suitable candidate for emerging point defect qubit applications, such as sub-nanoscale sensing in van der Waals heterostructure.

Methods

In this study, we use scanning transmission electron microscopy, three state-of-the-art electronic structure computational methods, see Supplementary Note 1, and exact spin dynamics simulations to investigate the VB2 defect.

Sample and STEM measurements

Chemical vapor deposition (CVD) was employed to grow hBN on copper substrates in our laboratory at the University of Texas. Copper (Cu) (25 μm, Alfa Aesar) was placed in a horizontal tube furnace and heated to 1000 °C under a gas flow of Ar and hydrogen (500 sccm, 0.35% hydrogen) for 60 min. Subsequently, the gas flow was adjusted to 80 sccm (22% hydrogen and 78% argon). Ammonia borane powder (>97%, Sigma Aldrich) was heated (80 °C) separately, and its vapor was delivered downstream to the Cu substrate to react. Growth occurred over 30 min, followed by rapid sample cooling. The hBN film was spin-coated with PMMA, etched in ammonium borane to remove the Cu, and then transferred to a TEM grid. The PMMA was removed by acetone overnight and then the samples were annealed in vacuum overnight. Annular dark-field scanning transmission electron microscopy (ADF-STEM) was performed using a JEOL ARM200CF STEM equipped with a CEOS probe corrector operated at an accelerating voltage of 80 kV. ADF-STEM with a low collection angle was acquired to increase the signal from light elements and discriminate B and N atoms as darker and brighter contrast. Dwell times of 5–20 μs and a pixel size of 0.006 nm px-1 were used for imaging with a convergence semi-angle of 22.5 mrad and a beam current of 35 pA. A camera length of 20 cm was used to provide a large collection of low-angle scattered electrons, increasing the contrast of hBN. ImageJ was used for line profile measurements and image analysis. Multislice image simulations were using QSTEM software with an accelerating voltage of 80 kV, a convergence semiangle of 21 mrad, a detector angle of 40–110 mrad, a spherical aberration of 0.001 nm, the chromatic aberration of 1 mm, and the defocus of -0.001 nm. The ADF-STEM images were colorized with Gem in lookup tables using ImageJ for better visibility.

DFT calculations

We apply density functional theory (DFT) calculations to study the energetic, ground state electronic, and spin properties, as well as the selected excited state properties of the VB2 defect. Throughout this work, we use a plane wave basis set of 450 eV and PAW[67] core potentials as implemented in VASP[68] and HSE06 hybrid exchange-correlation functional[69,70] with 0.32 exact exchange fraction[34]. For the charge transition level calculations we use a 768-atom supercell model of bulk hBN and the charge correction scheme by Freysoldt et al.[71]. For all the other calculations, we use a 162-atom single-sheet model of hBN embedding a single defect complex. In perpendicular direction, we use 30 Å supercell size. Furthermore, in single-layer calculations, we use DFT-D3 correction method of Grimme et al.[72]. We use a ZFS tensor calculation routine in the PAW formalism as implemented in VASP and spin contamination error correction as proposed in ref.[73]. We note that the spin contamination error is comparable with the largest element of the ZFS tensor, thus accurate ZFS parameters can only be achieved after decontamination. The DFT values are confirmed by NEVPT2 results for the unstrained configuration.

NEVPT2 calculations

The N-Electron Valence State Perturbation Theory (NEVPT2)[74] calculations were carried out using cc-pVDZ basis set[75] by the ORCA program package[76]. To this end, we employed a flake model of hBN, consisting of 38 B-, 40 N-, and 22 H-atoms. The underlining complete active space self-consistent field (CASSCF) calculations were performed based on the unrestricted Hartree-Fock orbitals, while we employed the CAS of 8 electrons and 8 orbitals and considered 6 triplet and 6 singlet states for the state-averaging. The spin-orbit coupling was introduced in the framework of quasi-degenerate perturbation theory, as implemented in ORCA.

DMRG calculations

DMRG[77] is a reference-free variational post-Hartree–Fock method which relies on an iterative local optimization scheme based on Schmidt decomposition[78]. The method is natively suitable for describing multi-reference problems of several dozens of strongly correlated orbitals[79,80]. As DMRG is capable of treating significantly larger completely active spaces compared to CASSCF-based methods, it can provide more robust results for strongly correlated problems.

DMRG computations are performed applying the Budapest DMRG package[81] restricting the spin of the target states to 0 and 1. In the DMRG truncation[80], the density matrix is formed of the equally weighted linear combination of the targeted spin-states, and the quantum information loss is preferred to be kept below threshold value $\chi = 10^{-5}$. Considering that only six defect orbitals display multireference character whereas the rest of the orbitals are found to be contributing to the dynamical correlation effects, a variant of the standard dynamically extended active space approach (DEAS)[82] is implemented and applied to initialize environment DMRG block states. Namely, the orbitals in the DMRG chain are arranged according to their localization on the defect atoms in descending order and the DMRG system block is optimized in the configuration space of the environment orbitals which is composed of determinants allowing up to all single orbital excitations. Contrary to the standard DEAS implementation, where environment block states tend to capture the essence of the multi-reference features of the corresponding orbitals, the modified initialization scheme focuses on the description of dynamical correlations of the complete environment from the initial DMRG micro iterations. The application of the novel DEAS protocol is favorable for the particular orbital space setups of current interest, i.e., orbitals display well-distinguished static or dynamical correlation character. In practice, the relative vertical energies are found to approach convergence within the first macro iterations of DMRG owing to the effective environmental initialization.

The input required for the DMRG calculations, i.e., Hamiltonian matrix elements, are expanded in the active space of Kohn-Sham DFT orbitals using program suite ORCA[83]. The spin-restricted Kohn-Sham orbitals are obtained assuming PBE correlation-exchange functional and fixing half-occupation on the highest-lying valence defect orbital pair. Matrix elements were computed by MRCC program[84,85] applying the complete active space protocol[86,87]. In our analysis, various active space setups were tested providing consistent excitation spectra, while the actual results are presented for 100 canonical orbitals filled with 188 electrons. The NEVPT and the DMRG calculations were performed on the same flake geometry.

Spin dynamics simulations

Exact spin dynamics simulations were carried out by using a spin Hamiltonian parametrized by our DFT spin coupling parameter calculations[88]. Magnetic resonance (MR) spectra were obtained by propagating the states of a four-spin model, including the triplet electron spin and three closest ^{14}N triplet nuclear spins, under an oscillating magnetic field of various frequencies and polarization direction. The MR figures show the change of the initial population of the $m_S = \pm 1$ states. The T_2^* coherence time was obtained by simulating the coherent oscillation of 178 electron spin-nuclear spin two spin systems. The overall coherence function is obtained as a product of the individual coherence functions[89]. The decaying coherence function of the electron spin was fitted by a Gaussian function to obtain the T_2^*. No nuclear spin nuclear spin flip-flops are included here.

Data availability

The data that support the findings of this study are available from the authors upon reasonable request.

Code availability

The codes associated with this manuscript are available from the corresponding author upon request.

Received: 27 December 2023; Accepted: 23 July 2024;

References

1. Degen, C., Reinhard, F. & Cappellaro, P. Quantum sensing. *Rev. Mod. Phys.* **89**, 035002 (2017).
2. Doherty, M. W. et al. The nitrogen-vacancy colour centre in diamond. *Phys. Rep.* **528**, 1–45 (2013).
3. Taylor, J. M. et al. High-sensitivity diamond magnetometer with nanoscale resolution. *Nat. Phys.* **4**, 810–816 (2008).
4. Michl, J. et al. Robust and Accurate Electric Field Sensing with Solid State Spin Ensembles. *Nano Lett*. **19**, 4904–4910 (2019).
5. Ovartchaiyapong, P., Lee, K. W., Myers, B. A. & Jayich, A. C. B. Dynamic strain-mediated coupling of a single diamond spin to a mechanical resonator. *Nat. Commun.* **5**, 4429 (2014).
6. Kucsko, G. et al. Nanometre-scale thermometry in a living cell. *Nature* **500**, 54–58 (2013).
7. DeVience, S. J. et al. Nanoscale NMR spectroscopy and imaging of multiple nuclear species. *Nat. Nanotechnol.* **10**, 129–134 (2015).
8. Bucher, D. B. et al. Quantum diamond spectrometer for nanoscale NMR and ESR spectroscopy. *Nat. Protoc.* **14**, 2707–2747 (2019).
9. Schmitt, S. et al. Submillihertz magnetic spectroscopy performed with a nanoscale quantum sensor. *Science* **356**, 832–837 (2017).
10. Boss, J. M., Cujia, K. S., Zopes, J. & Degen, C. L. Quantum sensing with arbitrary frequency resolution. *Science* **356**, 837–840 (2017).
11. Lovchinsky, I. et al. Nuclear magnetic resonance detection and spectroscopy of single proteins using quantum logic. *Science* **351**, 836–841 (2016).
12. Bluvstein, D., Zhang, Z., McLellan, C. A., Williams, N. R. & Jayich, A. C. B. Extending the quantum coherence of a nearsurface qubit by coherently driving the paramagnetic surface environment. *Phys. Rev. Lett.* **123**, 146804 (2019).
13. Dwyer, B. L. et al. Probing Spin Dynamics on Diamond Surfaces Using a Single Quantum Sensor. *PRX Quantum* **3**, 040328 (2022).
14. Tetienne, J.-P. Quantum sensors go flat. *Nature Physics* **17**, 1074–1075 (2021).
15. Vaidya, S., Gao, X., Dikshit, S., Aharonovich, I. & Li, T. Quantum sensing and imaging with spin defects in hexagonal boron nitride. *Advances in Physics: X* **8**, 2206049 (2023).

16. Kumar, P. et al. Magnetic imaging with spin defects in hexagonal boron nitride. *Phys. Rev. Applied* **18**, L061002 (2022).
17. Healey, A. J. et al. Quantum microscopy with van der waals heterostructures. *Nature Physics* **19**, 87–91 (2023).
18. Robertson, I. O. et al. Detection of paramagnetic spins with an ultrathin van der waals quantum sensor. *ACS Nano* **17**, 13408–13417 (2023).
19. Gao, X. et al. Quantum sensing of paramagnetic spins in liquids with spin qubits in hexagonal boron nitride. *ACS Photonics* **10**, 2894–2900 (2023).
20. Sasaki, K. et al. Magnetic field imaging by hBN quantum sensor nanoarray. *Appl. Phys. Lett.* **122**, 244003 (2023).
21. Exarhos, A. L., Hopper, D. A., Patel, R. N., Doherty, M. W. & Bassett, L. C. Magnetic-field-dependent quantum emission in hexagonal boron nitride at room temperature. *Nat. Commun.* **10**, 222 (2019).
22. Gottscholl, A. et al. Initialization and read-out of intrinsic spin defects in a van der Waals crystal at room temperature. *Nat. Mater.* **19**, 540–545 (2020).
23. Chejanovsky, N. et al. Single-spin resonance in a van der Waals embedded paramagnetic defect. *Nat. Mater.* **20**, 1079–1084 (2021).
24. Stern, H. L. et al. Room-temperature optically detected magnetic resonance of single defects in hexagonal boron nitride. *Nat. Commun.* **13**, 618 (2022).
25. Stern, H. L. et al. A quantum coherent spin in hexagonal boron nitride at ambient conditions. *Nat. Mater.* https://doi.org/10.1038/s41563-024-01887-z (2024).
26. Ivády, V. et al. Ab initio theory of the negatively charged boron vacancy qubit in hexagonal boron nitride. *npj Comput. Mater.* **6**, 41 (2020).
27. Sajid, A., Thygesen, K. S., Reimers, J. R. & Ford, M. J. Edge effects on optically detected magnetic resonance of vacancy defects in hexagonal boron nitride. *Commun. Phys.* **3**, 153 (2020).
28. Reimers, J. R. et al. Photoluminescence, photophysics, and photochemistry of the V_B^- defect in hexagonal boron nitride. *Phys. Rev. B* **102**, 144105 (2020).
29. Gottscholl, A. et al. Room temperature coherent control of spin defects in hexagonal boron nitride. *Sci. Adv.* **7**, eabf3630 (2021).
30. Liu, W. et al. Coherent dynamics of multi-spin the V_B^- center in hexagonal boron nitride. *Nat. Commun.* **13**, 5713 (2022).
31. Gottscholl, A. et al. Spin defects in hBN as promising temperature, pressure and magnetic field quantum sensors. *Nat. Commun.* **12**, 4480 (2021).
32. Benedek, Z. et al. Symmetric carbon tetramers forming spin qubits in hexagonal boron nitride. *npj Comput. Mater.* **9**, 187 (2023).
33. Sajid, A., Reimers, J. R. & Ford, M. J. Defect states in hexagonal boron nitride: Assignments of observed properties and prediction of properties relevant to quantum computation. *Phys. Rev. B* **97**, 064101 (2018).
34. Weston, L., Wickramaratne, D., Mackoit, M. & Alkauskas, A. & Van de Walle, C. G. Native point defects and impurities in hexagonal boron nitride. *Phys. Rev. B* **97**, 214104 (2018).
35. Abdi, M., Chou, J.-P., Gali, A. & Plenio, M. B. Color Centers in Hexagonal Boron Nitride Monolayers: A Group Theory and Ab Initio Analysis. *ACS Photonics* **5**, 1967–1976 (2018).
36. Sajid, A., Ford, M. J. & Reimers, J. R. Single-photon emitters in hexagonal boron nitride: a review of progress. *Rep. Prog. Phys.* **83**, 044501 (2020).
37. Turiansky, M. E., Alkauskas, A., Bassett, L. C. & Van de Walle, C. G. Dangling Bonds in Hexagonal Boron Nitride as Single-Photon Emitters. *Phys. Rev. Lett.* **123**, 127401 (2019).
38. Mackoit-Sinkevifçienfó, M., Maciaszek, M., Van de Walle, C. G. & Alkauskas, A. Carbon dimer defect as a source of the 4.1 eV luminescence in hexagonal boron nitride. *Appl. Phys. Lett.* **115**, 212101 (2019).
39. Hamdi, H., Thiering, G., Bodrog, Z., Ivády, V. & Gali, A. Stone-Wales defects in hexagonal boron nitride as ultraviolet emitters. *npj Comput. Mater.* **6**, 178 (2020).
40. Li, S. et al. Giant shift upon strain on the fluorescence spectrum of V_NN_B color centers in *h*-BN. *npj Quantum Inf.* **6**, 85 (2020).
41. Yim, D., Yu, M., Noh, G., Lee, J. & Seo, H. Polarization and Localization of Single-Photon Emitters in Hexagonal Boron Nitride Wrinkles. *ACS Appl. Mater. Interfaces* **12**, 36362–36369 (2020).
42. Ganyecz, Á. et al. First-principles theory of the nitrogen interstitial in hBN: a plausible model for the blue emitter. *Nanoscale* **16**, 4125–4139 (2024).
43. Barcza, G. et al. DMRG on Top of Plane-Wave KohnÄìSham Orbitals: A Case Study of Defected Boron Nitride. *J. Chem. Theory Comput.* **17**, 1143–1154 (2021).
44. Smart, T. J., Li, K., Xu, J. & Ping, Y. Intersystem crossing and exciton-defect coupling of spin defects in hexagonal boron nitride. *npj Comput. Mater.* **7**, 59 (2021).
45. Strand, J., Larcher, L. & Shluger, A. L. Properties of intrinsic point defects and dimers in hexagonal boron nitride. *J. Phys.: Condens. Matter* **32**, 055706 (2019).
46. Park, H. et al. Atomically Precise Control of Carbon Insertion into hBN Monolayer Point Vacancies using a Focused Electron Beam Guide. *Small* **17**, 2100693 (2021).
47. Toledo, J. R. et al. Electron paramagnetic resonance signature of point defects in neutron-irradiated hexagonal boron nitride. *Phys. Rev. B* **98**, 155203 (2018).
48. Fischer, M. et al. Controlled generation of luminescent centers in hexagonal boron nitride by irradiation engineering. *Sci. Adv.* **7**, eabe7138 (2021).
49. Kianinia, M., White, S., Fröch, J. E., Bradac, C. & Aharonovich, I. Generation of Spin Defects in Hexagonal Boron Nitride. *ACS Photonics* **7**, 2147–2152 (2020).
50. Ghaderzadeh, S., Kretschmer, S., Ghorbani-Asl, M., Hlawacek, G. & Krasheninnikov, A. V. Atomistic Simulations of Defect Production in Monolayer and Bulk Hexagonal Boron Nitride under Low- and High-Fluence Ion Irradiation. *Nanomaterials* **11**, 1214 (2021).
51. Gao, X. et al. Femtosecond Laser Writing of Spin Defects in Hexagonal Boron Nitride. *ACS Photonics* **8**, 994–1000 (2021).
52. Chen, Y. & Quek, S. Y. Photophysical Characteristics of Boron Vacancy-Derived Defect Centers in Hexagonal Boron Nitride. *J. Phys. Chem. C.* **125**, 21791–21802 (2021).
53. Gali, A., Janzén, E., Deák, P., Kresse, G. & Kaxiras, E. Theory of spin-conserving excitation of the N-V^- center in diamond. *Phys. Rev. Lett.* **103**, 186404 (2009).
54. Alkauskas, A. & Yan, Q. & Van de Walle, C. G. First-principles theory of nonradiative carrier capture via multiphonon emission. *Phys. Rev. B* **90**, 075202 (2014).
55. Wu, F., Smart, T. J., Xu, J. & Ping, Y. Carrier recombination mechanism at defects in wide band gap two-dimensional materials from first principles. *Phys. Rev. B* **100**, 081407 (2019).
56. Turiansky, M. E. et al. Nonrad: Computing nonradiative capture coefficients from first principles. *Comput. Phys. Commun.* **267**, 108056 (2021).
57. Fröch, J. E. et al. Purcell Enhancement of a Cavity-Coupled Emitter in Hexagonal Boron Nitride. *Small* **18**, 2104805 (2022).
58. Li, K., Smart, T. J. & Ping, Y. Carbon trimer as a 2 eV single-photon emitter candidate in hexagonal boron nitride: a first-principles study. **6**, L042201 (2022).
59. Vogl, T., Lu, Y. & Lam, P. K. Room temperature single photon source using fiber-integrated hexagonal boron nitride. *J. Phys. D: Appl. Phys.* **50**, 295101 (2017).
60. Li, X., Scully, R. A., Shayan, K., Luo, Y. & Strauf, S. Near-Unity Light Collection Efficiency from Quantum Emitters in Boron Nitride by

Coupling to Metallo-Dielectric Antennas. *ACS Nano* **13**, 6992–6997 (2019).

61. Huseynov, E. M. et al. EPR spectroscopy of neutron irradiated nanocrystalline boron nitride (h-BN) particles. *Ceram. Int.* **47**, 7218–7223 (2021).
62. Miao, K. C. et al. Universal coherence protection in a solid-state spin qubit. *Science* **369**, 1493–1497 (2020).
63. Bucher, D. B., Glenn, D. R., Park, H., Lukin, M. D. & Walsworth, R. L. Hyperpolarization-Enhanced NMR Spectroscopy with Femtomole Sensitivity Using Quantum Defects in Diamond. *Phys. Rev. X* **10**, 021053 (2020).
64. Udvarhelyi, P., Shkolnikov, V. O., Gali, A., Burkard, G. & Pályi, A. Spin-strain interaction in nitrogen-vacancy centers in diamond. *Phys. Rev. B* **98**, 075201 (2018).
65. Dréau, A. et al. Avoiding power broadening in optically detected magnetic resonance of single NV defects for enhanced dc magnetic field sensitivity. *Phys. Rev. B* **84**, 195204 (2011).
66. Pham, L. M. Magnetic Field Sensing with Nitrogen-Vacancy Color Centers in Diamond. https://dash.harvard.edu/handle/1/11051173 (2013).
67. Blöchl, P. E. Projector augmented-wave method. *Phys. Rev. B* **50**, 17953–17979 (1994).
68. Kresse, G. & Hafner, J. Ab initio molecular-dynamics simulation of the liquid-metalÄìamorphous-semiconductor transition in germanium. *Phys. Rev. B* **49**, 14251–14269 (1994).
69. Heyd, J., Scuseria, G. E. & Ernzerhof, M. Hybrid functionals based on a screened coulomb potential. *J. Chem. Phys.* **118**, 8207 (2003).
70. Heyd, J., Scuseria, G. E. & Ernzerhof, M. Erratum: Hybrid functionals based on a screened coulomb potential. *J. Chem. Phys.* **124**, 219906 (2006).
71. Freysoldt, C., Neugebauer, J. & Van de Walle, C. G. Fully Ab Initio finite-size corrections for charged-defect supercell calculations. *Phys. Rev. Lett.* **102**, 016402 (2009).
72. Grimme, S., Antony, J., Ehrlich, S. & Krieg, H. A consistent and accurate ab initio parametrization of density functional dispersion correction (DFT-D) for the 94 elements H-Pu. *J. Chem. Phys.* **132**, 154104 (2010).
73. Biktagirov, T., Schmidt, W. G. & Gerstmann, U. Spin decontamination for magnetic dipolar coupling calculations: Application to high-spin molecules and solid-state spin qubits. *Phys. Rev. Res.* **2**, 022024 (2020).
74. Angeli, C., Cimiraglia, R., Evangelisti, S., Leininger, T. & Malrieu, J.-P. Introduction of n-electron valence states for multireference perturbation theory. *J. Chem. Phys.* **114**, 10252–10264 (2001).
75. Dunning, T. H. Gaussian basis sets for use in correlated molecular calculations. I. The atoms boron through neon and hydrogen. *J. Chem. Phys.* **90**, 1007–1023 (1989).
76. Neese, F. Software update: the orca program system, version 4.0. *Wiley Interdiscip. Rev.: Comput. Mol. Sci.* **8**, e1327 (2018).
77. White, S. R. & Martin, R. L. Ab initio quantum chemistry using the density matrix renormalization group. *J. Chem. Phys.* **110**, 4127–4130 (1999).
78. Schollwöck, U. The density-matrix renormalization group. *Rev. Mod. Phys.* **77**, 259–315 (2005).
79. Olivares-Amaya, R. et al. The ab-initio density matrix renormalization group in practice. *J. Chem. Phys.* **142**, 034102 (2015).
80. Szalay, S. Z. et al. Tensor product methods and entanglement optimization for ab initio quantum chemistry. *Int. J. Quantum Chem.* **115**, 1342–1391 (2015).
81. Legeza, Ö., Veis, L. & Mosoni, T. QC-DMRG-Budapest, a program for quantum chemical DMRG calculations (2020).
82. Legeza, O. & Sólyom, J. Optimizing the density-matrix renormalization group method using quantum information entropy. *Phys. Rev. B* **68**, 195116 (2003).
83. Neese, F. The orca program system. *Wiley Interdiscip. Rev.: Comput. Mol. Sci.* **2**, 73–78 (2012).
84. Kallay, M.et al. MRCC, a quantum chemical program suite. www.mrcc.hu (2020).
85. Kallay, M. et al. The MRCC program system: Accurate quantum chemistry from water to proteins. *J. Chem. Phys.* **152**, 074107 (2020).
86. Jensen, F. *Introduction to Computational Chemistry*. (John Wiley and Sons, Inc, Hoboken, NJ, USA, 2006).
87. Barcza, G. et al. DMRG on Top of Plane-Wave Kohn-Sham Orbitals: A Case Study of Defected Boron Nitride. *J. Chem. Theory Comput.* **17**, 1143–1154 (2021).
88. Ivády, V., Abrikosov, I. A. & Gali, A. First principles calculation of spin-related quantities for point defect qubit research. *npj Comput. Mater.* **4**, 76 (2018).
89. Seo, H. et al. Quantum decoherence dynamics of divacancy spins in silicon carbide. *Nat. Commun.* **7**, 12935 (2016).

Acknowledgements

This research was supported by the National Research, Development, and Innovation Office of Hungary within the Quantum Information National Laboratory of Hungary (Grant No. 2022-2.1.1-NL-2022-00004) and within grants FK 135496 and FK 145395. We acknowledge support from the Knut and Alice Wallenberg Foundation through WBSQD2 project (Grant No. 2018.0071). Support from the Swedish Government Strategic Research Area SeRC and the Swedish Government Strategic Research Area in Materials Science on Functional Materials at Linköping University (Faculty Grant SFO-Mat-LiU No. 2009 00971) is gratefully acknowledged. A.G. acknowledges the support from the European Commission for the project QuMicro (Grant No. 101046911) and SPINUS (Grant No. 101135699). Ö.L. acknowledges financial support from the Hungarian National Research, Development and Innovation Office (NKFIH) through Grants No. K134983, TKP2021-NVA-04, Quantum Information National Laboratory of Hungary, the Hans Fischer Senior Fellowship programme funded by the Technical University of Munich Institute for Advanced Study, and by the Center for Scalable and Predictive methods for Excitation and Correlated phenomena (SPEC), funded as part of the Computational Chemical Sciences Program FWP 70942, by the U.S. Department of Energy (DOE), Office of Science, Office of Basic Energy Sciences, Division of Chemical Sciences, Geosciences, and Biosciences at Pacific Northwest National Laboratory. A.P. and G.T. were supported by the János Bolyai Research Scholarship of the Hungarian Academy of Sciences. G.T. also acknowledges the ÚNKP-20-5 New National Excellence Program for Ministry Innovation and Technology from the source of the National Research, Development and Innovation Fund. The computations were enabled by resources provided by the National Academic Infrastructure for Supercomputing in Sweden (NAISS) and the Swedish National Infrastructure for Computing (SNIC) at the National Supercomputer Centre (NSC) partially funded by the Swedish Research Council through grant agreements no. 2022-06725 and no. 2018-05973. We acknowledge KIFÜ for awarding us access to computational resources based in Hungary.

Author contributions

The DFT calculations were performed by R.B., V.I., O.B.L., and G.T. with inputs from A.G. and I.A.A. The DFT-CAS-DMRG and NEVPT2 calculations were performed by G.B. and A.P., respectively, with inputs from V.I., A.G., and Ö.L. The STEM measurements were carried out by H.P. and J.H.W. The spin dynamics simulations were carried out by V.I. The results were analyzed with contributions from all authors. V.I. wrote the manuscript with inputs from the coauthors.

Funding

Open access funding provided by Eötvös Loránd University.

Competing interests

The authors declare no competing interests.

Additional information

Supplementary information The online version contains supplementary material available at https://doi.org/10.1038/s41524-024-01361-z.

Correspondence and requests for materials should be addressed to Adam Gali or Viktor Ivády.